Four-decade record of pervasive grounding line retreat along the Bellingshausen margin of West Antarctica

Four-decade record of pervasive grounding line retreat along the Bellingshausen margin of West Antarctica

Frazer D.W. Christie[1], Robert G. Bingham[1], Noel Gourmelen[1], Simon F.B. Tett[1], Atsuhiro Muto[2]

[1] School of GeoSciences, University of Edinburgh, UK

[2] Department of Earth and Environmental Science, Temple University, USA

Corresponding Author: Frazer Christie, F.Christie@ed.ac.uk

Key Points

- Grounding line change mapped along Bellingshausen margin of West Antarctica with Landsat and InSAR from 1975 to 2015
- Results show majority of grounding line retreated along entire margin implicating ocean-forced dynamic thinning
- Grounding line at Venable Ice Shelf currently pinned but potential for retreat as at Pine Island Glacier

This article has been accepted for publication and undergone full peer review but has not been through the copyediting, typesetting, pagination and proofreading process which may lead to differences between this version and the Version of Record. Please cite this article as doi: 10.1002/2016GL068972

Abstract

Changes to the grounding line, where grounded ice starts to float, can be used as a remotely-sensed measure of ice-sheet susceptibility to ocean-forced dynamic thinning. Constraining this susceptibility is vital for predicting Antarctica's contribution to rising sea levels. We use Landsat imagery to monitor grounding line movement over four decades along the Bellingshausen margin of West Antarctica, an area little monitored despite potential for future ice losses. We show that ~65% of the grounding line retreated from 1990-2015, with pervasive and accelerating retreat in regions of fast ice flow and/or thinning ice shelves. Venable Ice Shelf confounds expectations in that despite extensive thinning, its grounding line has undergone negligible retreat. We present evidence that the ice shelf is currently pinned to a sub-ice topographic high which, if breached, could facilitate ice retreat into a significant inland basin, analogous to nearby Pine Island Glacier.

Index Terms and Keywords

0728 Ice shelves

0730 Ice streams

0758 Remote sensing

6924 Interferometry (1207, 1209, 1242)

9310 Antarctica (4207)

Landsat, InSAR, grounding line, Pine Island Glacier, Antarctica, ice-ocean interaction

1. Introduction

Satellite remote sensing of the Antarctic Ice Sheet over the last 25 years has revealed trends of ice loss that are especially pronounced around its coastline [*Shepherd* et al., 2010; *McMillan* et al., 2014]. Manifested by thinning of floating ice [e.g. *Paolo* et al. 2015], dynamic thinning of grounded ice [e.g. *Pritchard* et al., 2009], and rapid retreat of grounding lines [e.g. *Rignot* et al., 2014], these ice losses form one of the largest components of contemporary global sea-level rise [*Shepherd* et al., 2012; *Vaughan* et al., 2013]. However, the processes by which they occur remain imperfectly understood. The spatiotemporal distribution of the observed ice losses strongly suggests a forcing that initiates at ice-sheet margins [*Pritchard* et al., 2012], and several recent studies have attributed the dynamic thinning of grounded ice to the thinning of ice shelves [*Jenkins* et al. 2010; *MacGregor* et al. 2012; *Pritchard* et al., 2012]. This is, in turn, a possible consequence of the ingress of relatively warm circumpolar deep water (hereafter CDW) across the continental shelf to the sub-ice-shelf cavity [*Walker* et al., 2007; *Jacobs* et al., 2011; *Bingham* et al., 2012]. These processes are hypothesized to be responsible for ice losses from the sectors of West Antarctica that drain to the Amundsen and Bellingshausen Seas [*Rignot* et al., 2008; *Pritchard* et al., 2012; *Bingham* et al., 2012] but, while the former has received considerable observational and modelling attention [*Payne* et al., 2004; *Shepherd* et al., 2004; *Scott* et al., 2009; *Joughin* et al., 2012; *Favier* et al., 2014; *Joughin* et al., 2014; *Rignot* et al., 2014; *Seroussi* et al., 2014; *Goldberg* et al., 2015], few observations of glacial change in the Bellingshausen Sea Sector (hereafter BSS) have been published.

It is important to generate improved records of glacial change in the BSS for several reasons. First, the estimated mass lost from the region between 1992 and 2006 (~49 Gt yr^{-1}) comprised

35% of total mass loss from the West Antarctic Ice Sheet [*Rignot* et al., 2008], second only to contributions from the Amundsen Sea Sector (~64 Gt yr^{-1}; 46% of total loss). Second, a recent study has suggested that mass loss since 2009 has been particularly significant, and that the region may have destabilised [*Wouters* et al., 2015]. Third, although studies from the neighbouring Amundsen Sea Sector are offering insights into dynamic thinning and its possible oceanic forcing, the scarcity of glacial-change records and supporting information in the BSS (such as sub-shelf and grounded-ice geometry; physical oceanographic data) make it difficult to assess whether changes in the BSS have occurred at similar or different timescales to those in the Amundsen Sea Sector, potentially implicating different or additional forcing or feedbacks.

In order to improve our understanding of glacial change across this region, we generated a comprehensive dataset of grounding line (hereafter GL) positional change along the Bellingshausen Sea coastline for the period 1975-2015. We exploited a combination of optical and radar satellite imagery to map GL positions at approximately 5- to 10-year intervals. We find that, over this 40-year period, almost the entire length of the coastline has experienced GL retreat, with the greatest retreat typically occurring in regions containing deeply-bedded, fast-flowing outlet glaciers and ice streams. We suggest that this pervasive trend implicates widespread access of CDW to the Bellingshausen glacial margin, so that even despite relatively high accumulation inland, the mass balance for much of the region is strongly negative. Only in some special cases has the GL remained relatively stable in position or undergone advance, probably as a result of local topographic pinning that is likely to be overcome with continued regional oceanic forcing.

2. Methodology

2.1 Landsat grounding line mapping

We used Landsat optical satellite imagery as our primary data source due to its unmatched spatial-temporal coverage compared with other remote sensing datasets covering the BSS. The position of the GL was mapped from these images at 5- to 10-year intervals between 1975 and 2015 as follows.

Referring to the conceptual diagram of *Fricker* et al. [2009; their Fig. 2], the "true" GL (where ice decouples from the bed and begins to float due to tidal forcing; their "*G*") cannot be identified reliably with static, optical imagery (such as Landsat). Instead, using Landsat imagery, the most suitable proxy for *G* is the break-in-slope, otherwise known as the "inflexion point" [hereafter I_b; after notation in *Fricker* et al., 2009], which is defined as the most seaward continuous slope break detectable in satellite imagery [*Brunt* et al., 2010; following *Scambos* et al., 2007]. Situated within close proximity to *G*, I_b appears as a clearly defined shadow-like change in image brightness on optical imagery [cf. *Bindschadler* et al., 2011] (Figure S1).

Using GIS tools on georeferenced multispectral Landsat scenes (Table S1), we digitised the position of I_b at approximately 50-100 m intervals along the BSS coastline and coastal islands for years 1975, c.1985, c.1990, 2000, 2005, 2010 and 2015. The majority of scenes used were acquired during austral summer (January/February). For c.1985 and c.1990 we utilized data from $\pm$ 2 years where 1985/1990 scene spatial coverage was poor. Throughout the study, only images with cloud cover $\leq$ 10% were utilized. The launch failure of Landsat 6 in 1993 was

responsible for a hiatus in Landsat acquisitions throughout the mid-1990s, precluding any mapping of results for c.1995.

Using a similar I_b mapping technique to that employed by *Bindschadler* et al. [2011], we estimate positional uncertainty (1σ) of I_b = ~103 m for most of the BSS coastline (206 m for 1975 mapping), with the exception of the fast-flowing Ferrigno Ice Stream, where I_b (1σ) = ~502 m (cf. *Bindschadler* et al. [2011]; see Text S1, Table S2). In terms of the principal objective of this paper, which is to monitor changes in the position of the GL across 5-year intervals, any imprecision in locating I_b (on the order of 10^2 m) is outweighed by changes in its position after 5 years (on the order of 10^2-10^3 m). This uncertainty broadly matches the positional uncertainty associated with other remote sensing techniques, such as Interferometric Synthetic Aperture Radar [InSAR; cf. *Rignot* et al., 2011].

It is important to recognise that under some conditions the use of I_b as a proxy for the GL may fail [cf. Fricker et al., 2009]. The typical contexts in which I_b makes a poor indicator are in areas of fast ice flow, where subglacial bed and surface slopes are shallow and I_b is difficult to define; and/or in ice plains, where multiple breaks-in-slope may be present around the grounding zone, or where the break-in-slope may decouple substantially from the location of the "true" GL with tidal variability [cf. Corr et al., 2001; Fricker & Padman, 2006; Fricker et al., 2009; Brunt et al., 2011]. Therefore, to ascertain the utility of Landsat for monitoring GL change, we additionally employed InSAR mapping techniques to monitor the nature and configuration of grounding zones throughout the BSS, and to identify the potential presence of ice plains in this sector.

2.2 Interferometric Synthetic Aperture Radar (InSAR)

Where Synthetic Aperture Radar (SAR) observations have been acquired, it is possible to map the inland limit of tidal flexure acting on the grounding zone, *F*, directly [e.g. *Fricker* et al., 2009; their Figure 2; *Brunt* et al., 2010; *Rignot* et al., 2011]. We applied interferometry to SAR data acquired from the European Space Agency's ERS-1 and ERS-2 satellites to delineate *F* along the BSS coastline between 1992 and 2011. The data consist of SAR scenes acquired in 1992, 1994, 1996 and 2011 (Table S4), and the generated interferograms have temporal baselines of either 1 day (1996) or 3 days (1992, 1994, 2011).

Following *Park* et al. [2013], we employed a double-differential InSAR processing technique, whereby we differenced consecutive interferograms, corrected for the effects of surface topography using a resampled version of the Bedmap2 surface digital elevation model [*Fretwell* et al., 2013], in order to remove signals related to ice flow and reveal vertical surface motion due to tidal flexure acting upon the grounding zone from floating ice shelves. Such motion, which is represented in double-differenced interferograms as a band of closely spaced fringes across the grounding zone (Figure S2), reveals *F* as the landward limit of tidally-induced vertical ice motion.

To quantify the positional uncertainty of InSAR-derived *F*, we compared the tidally-variable location of *F* from multiple double-differenced interferograms, where possible across multiple epochs. From this, we estimated tidally-induced variation in *F* to range from ~±100 m across areas of steeply-bedded, shoaling subglacial topography to ≤ ~±300 m across deeply-grounded outlet glaciers with shallow bed slopes. These values align with positional accuracy estimations in other areas of Antarctica (cf. *Rignot* et al. [2011]; *Park* et al. [2013]).

Our determination of InSAR-derived *F* confirms the absence of ice plains and other complex ice-shelf geometries along the BSS. Therefore, unlike for other regions of Antarctica where optical based I_b mapping campaigns have been prone to failure (e.g. *Fricker* et al. [2009]; *Brunt* et al. [2011]), we are confident that Landsat-derived I_b acts as a good proxy for the GL in this sector.

2.3 Quantifying grounding line position retreat/advance

To quantify GL advance or retreat over epochs, we defined the 2015 Landsat-mapped I_b as a baseline. We partitioned this baseline into 30-km segments, and at the limit of each segment defined a normal extending infinitely both landward and seaward from the baseline. These normals intercept the mapped I_b for all years. To calculate advance or retreat of I_b for any 30 km segment of coastline over any period [2015 – *y*], where *y* = year of interest, we defined a polygon bounded by the 2015 baseline, the mapped I_b for year *y*, and the two intercepting normals. We then summed the areas of each polygon, in each case defining whether I_b had retreated or advanced over the epoch of interest; and then divided by 30 km to convert the final figure into a magnitude of I_b advance/retreat over each epoch of interest (see Text S2 and Data Set S1).

3. Results

[INSERT FIG. 1 & CAPTION]

Figure 1 shows that the most significant changes to the GL position between 1990 and 2015 are located at Ferrigno and Fox Ice Streams (-2.77 ± 0.50 km and -1.79 ± 0.14 km

respectively) and Stange Ice Shelf (-0.92 ± 0.14 km). Since 1990, net GL retreat has been widespread along the BSS coastline and around Thurston Island, and has occurred along much of the margin draining to the Amundsen Sea between the Cosgrove Ice Shelf and Pine Island Glacier. In total, between 1990 and 2015, 65.4% of the GL along the mainland BSS experienced net retreat, and only 7.4% net advance. Over the same epoch, 29.3% of the GL around Thurston Island experienced net retreat, and only 1.8% net advance. Most of the detectable retreat around Thurston Island occurred along its southern (Abbot Ice Shelf-facing) margin; change along its northern margin was often not possible to discern outside Landsat 1σ-error bounds. Figure 1 also shows the tendency for the greatest GL retreat to be associated with regions of fast-flowing, likely deeply-grounded ice.

[INSERT FIG. 2 & CAPTION]

Partitioning the observations into change over 5- to 10-year epochs (Figure 2), the most comprehensive coverage along the entire coastline begins in 1990, from which time it is clear that the pace of GL retreat at Eltanin Bay has been persistently high. There (for segments 22-26 in Data Set S1; locations of Ferrigno and Fox Ice Streams), the GL retreated on average 0.45 ± 0.14 km (at a rate of 45 ± 27 m yr^{-1}) from 1990-2000, 0.46 ± 0.14 km (92 ± 27 m yr^{-1}) from 2000-2005, 0.50 ± 0.14 km (100 ± 27 m yr^{-1}) from 2005-2010, and most recently 0.52 ± 0.14 km (104 ± 27 m yr^{-1}) from 2010-2015.

Where data exist from 1975 or 1985 onwards, some sites experienced relatively fast GL retreat in the earlier epochs we have analysed, followed by slower retreat or undetectable change, and then increased retreat towards the present-day. One example is the western Stange Ice Shelf, where the GL at Berg Ice Stream retreated 0.54 ± 0.14 km (36 ± 27 m yr^{-1})

between 1975-1990, remained stable within Landsat error bounds between 1990-2010, then retreated 0.24 ± 0.14 km (48 ± 27 m yr^{-1}) between 2010 and 2015. Further west, between latitudes 93°W (eastern Abbot Ice Shelf) and 87°W (Wiesnet Ice Stream/Venable Ice Shelf) we also find notable GL retreat between 1985 and 1990 relative to all intervening epochs until 2010-2015. In 2010-2015, the GL along eastern Abbot Ice Shelf then experienced a renewed retreat (distance 0.31 ± 0.14 km; rate 62 ± 27 m yr^{-1}; segments 38-40 in Data Set S1), while the GL also experienced a detectable minor retreat between the Wiesnet and Williams Ice Streams feeding Venable Ice Shelf (0.23 ± 0.14 km at 45 ± 27 m yr^{-1}; segments 30 in Data Set S1).

4. Discussion

Our observations demonstrate that since 1975/1985 there has been a net retreat of the grounding line along almost all of the BSS (Figure 1; Figure 2; Figure S3), demonstrating a pervasive trend of ice response along the whole Bellingshausen Sea coastline. Within this trend, several further phenomena are notable. First, both the greatest retreat (Figure 1) and the greatest increase in GL retreat rates from the 1990s to the present (Figure 2) have occurred along the eastern BSS coast, incorporating the glaciers and ice streams draining to Eltanin Bay and Stange Ice Shelf. Second, observed retreat rates in the BSS have varied over time across different locations. Third, whilst the ice streams feeding the Venable Ice Shelf have experienced limited retreat over the last three decades, retreat rates do not align with the more pronounced glaciological changes occurring more widely across the BSS and nearby Amundsen Sea Embayment.

Ferrigno Ice Stream, where we have observed the greatest net GL retreat from 1990-2015 (Figure 1), has been highlighted in several previous studies as a region of especially pronounced ice-surface lowering and inferred ice loss [*Rignot* et al., 2008; *Pritchard* et al., 2009; *McMillan* et al., 2014; *Wouters* et al., 2015]. *Bingham* et al. [2012] suggested that Ferrigno Ice Stream is currently undergoing dynamic thinning as a consequence of the ingress of warm CDW to its ice front along Belgica Trough, a continental-shelf transecting depression formed during glacial maximum conditions [*Ó Cofaigh* et al., 2005; Figure 1]. Here we add that the GL of Ferrigno Ice Stream has been retreating since at least 1975 (Figure S3), and that the neighbouring Alison and Fox Ice Streams have been retreating since at least 1990 (Figure 2, Figure S3; no data exist beforehand), suggesting that the effects of CDW forcing have been prevalent in Eltanin Bay for at least twenty-five years. The region's vulnerability is likely exacerbated by shallow bed slopes observed near/at the grounding zones of this sector as compared to neighbouring regions [*Bingham* et al., 2012; Figure 3], in addition to the lack of an ice shelf to provide a backstress to grounded ice. As such, the general absence of ice shelves throughout this region further signals potentially longstanding ingress of CDW to the bay [*Holland* et al., 2010]. It is also notable that GL retreat here has occurred at a greater rate over the last decade (2005-2015) than previously (Figure 2); a trend which is in general agreement with those reported by *Rignot* et al. [2008], *Pritchard* et al. [2009], *McMillan* et al. [2014] and *Wouters* et al. [2015] with respect to other indicators of accelerating glacial response over this period. Moreover, following the approach of *Park* et al. [2013], GL thinning estimates obtained from our 2010-2015 GL retreat rates are consistent with estimates of inland thinning produced through CryoSat-2 swath processing over the same observational period (Figure S4, Text S3). Analysis of CryoSat-2-derived rates of surface elevation change reveals extensive thinning inland of the Fox and Ferrigno GLs (max. -6.40 m yr^{-1}, $\sigma = \pm 0.49$ m yr^{-1}), which compares well with our Landsat-derived theoretical

thinning estimations (mean = -5.96 m yr^{-1}, σ = ±3.40 m yr^{-1}; Figure S4, Text S3). There is therefore mounting evidence that the Eltanin Bay component of the BSS is not only prone to marine instability, but is already experiencing the early stages of retreat, like nearby Pine Island Glacier [cf. *Jenkins* et al. 2010].

[INSERT FIG. 3 & CAPTION]

Ice flowing into Stange Ice Shelf is also remarkable for experiencing extensive GL retreat since 1975 (Figure 2; Figure S3). The pervasiveness and magnitude of GL retreat there suggest that the ice shelf's capacity to buttress the contributing glaciers' flow has been diminishing as a likely consequence of ice-shelf thinning. Thinning across Stange Ice Shelf has been inferred from radar altimetry between 1992 and 2008 [*Holt* et al., 2014] and 1994 to 2012 [*Paolo* et al., 2015], though the rates have varied considerably with location and time [*Holt* et al., 2014]. The greatest thinning of Stange Ice Shelf has consistently occurred on its westward flanks [*Paolo* et al., 2015], but where the western Stange Ice Shelf meets the BSS GL (at Berg Ice Stream, Figure 1), GL retreat between 1975 and 2015 has been suppressed relative to further east (Figure 1; Figure 2). An explanation for this apparent discrepancy lies in the geometry of the ice bed at the relative locations: a radar profile approximately following the GL along Stange Ice Shelf hints at a shallower bed, or bed protuberance, underlying Berg Ice Stream's GL compared with at the more eastern outlets feeding the ice shelf (notably Lidke Ice Stream; Figure 3). With respect to the temporal changes in GL retreat, the oscillatory nature of the observed retreat rates (i.e. instances of large-to-small-to-large retreat through time) corresponds with the suppression of ice-shelf thinning *Paolo* et al. [2015] measured for all BSS ice shelves from ~2000-2008 relative to the periods immediately preceding and succeeding it (i.e. 1994-2000; 2008-2012). That the GL retreat and ice-shelf

thinning trends follow a similar oscillatory pattern lends credence to the hypothesis that regional changes on and around Stange Ice Shelf are, as with Ferrigno Ice Stream, fundamentally driven by persistent CDW access to the ice-shelf cavity [cf. *Holt* et al., 2014]. Though the sub-shelf and near-ice-front bathymetry of Stange Ice Shelf remain poorly surveyed [*Graham* et al., 2011], the observed behaviour of the GL retreat is strongly suggestive that the ice shelf is underlain by a north-south-aligned deep bathymetric trough that allows CDW to flow from the Ronne Entrance beneath Stange Ice Shelf to the GL.

GL retreat observed along the margins of the Abbot and Cosgrove Ice Shelves, as well as on southern Thurston Island, has occurred in locations further from known regions of CDW ingress (Figure 1). However, most of the larger retreats in the western Bellingshausen Sea (e.g. Rosanova Glacier, Figure 1) took place where Bedmap2 [*Fretwell* et al., 2013] indicates deeply bedded grounding zones. Similar to Stange Ice Shelf, parts of this coastline exhibited some oscillatory behaviour, with the margin between 100°W and 94°W (including Rosanova Glacier) and 93°W and 89°W (eastern Abbot Ice Shelf) experiencing higher retreat in 1985-90 relative to any subsequent epoch until 2010-15, when further enhanced GL retreat was observed. Given these observations, we hypothesize that CDW-forced dynamic thinning is also occurring in many of these locations. The dearth of bathymetric data in the western BSS [*Graham* et al., 2011] leaves open the possibility that throughout the length of the Abbot Ice Shelf, there may be undiscovered access routes for CDW to reach GLs here. Indeed, there is compelling evidence from recently acquired aerogeophysical data that a tectonically-rifted basin underlies the majority of the ice shelf [*Cochran* et al., 2014], and that deep topographic lows may be present near the grounding lines of the eastern Abbot Ice Shelf (Figure 3).

The few cases of GL advance we have observed across the BSS are located where ice at the GL is thin and slow, and the bed steepens/shoals inland (Figure 1). For example, the small advances at King Peninsula (Figure 1; segments 59, 61 and 62 in Data Set S1) occurred where ice thickness is ~200-400 m and modelled depth-averaged ice velocities are < 100 m yr^{-1}. In these locations, we hypothesise that the grounding zone geometry is relatively immune to dynamic thinning, and that the GL subsequently advanced in response to the high rates of accumulation experienced by the BSS [*Lenaerts* et al., 2012].

Finally, we highlight the minor GL retreat experienced by the ice streams feeding Venable Ice Shelf, which appears at odds with recent observations that this ice shelf has experienced significant thinning since the 1990s [e.g. *Pritchard* et al., 2012; *Paolo* et al., 2015], likely forced by CDW accessing the ice-shelf cavity via Belgica Trough [see Figure 1; *Graham* et al., 2011]. Indeed, *Paolo* et al. [2015] report Venable Ice Shelf as having experienced the most dramatic thickness reduction of all Antarctic ice shelves over the period 1994-2012, thinning at a mean rate of 36.1 ± 4.4 m $decade^{-1}$ to 82% of its 1994 thickness. Despite this exceptional thinning, and known deep bathymetry to the ice shelf's northern margin that potentially connects to the CDW-flooded Belgica Trough, we have observed only limited GL retreat at this location. Here, the largest GL change occurred between 1985 and 1990 (0.22 km of retreat at 45 m yr^{-1}; segments 30-32 in Data Set S1); and little change in GL position has been observed since. As noted previously, a small retreat is apparent in 2010-2015, but its magnitude (total 0.11 km) is insufficient to support a case that it represents a significant upward or persistent trend in retreat rate [cf. *Wouters* et al., 2015]. We propose that the discrepancy between oceanic forcing and suppressed GL response observed over the last two decades is a result of the specific bed geometry at/around the grounding zone, presently acting to pin the GL to its current location. Radar data acquired by NASA Operation

IceBridge suggest that the bed along the Venable Ice Shelf GL is relatively shallow, including where Wiesnet and Williams Ice Streams feed into the ice shelf (Figure 3). Significantly, however, where the same surveys profiled ice thickness inland, they partly captured a deep basin underlying Williams Ice Stream from ~40 km inland. A subsequent airborne gravity survey of this basin, reaching a further 50 km inland (Figure 3), showed free-air gravity anomalies 80-100 mGal lower than the surroundings, comparable to those observed over Ferrigno Ice Stream [*Bingham* et al., 2012], indicating the likely existence of a significant, deeply-bedded basin lying beneath Williams Ice Stream. This feature is not identified in Bedmap2 [*Fretwell* et al., 2013], which did not incorporate these gravity-anomaly data, and renders the setting analogous to both Ferrigno Ice Stream and Pine Island Glacier, which are already experiencing active dynamic thinning. Moreover, in the case of Pine Island Glacier, the current trends are a likely response to the floating section having become ungrounded from a previously longstanding pinning point [*Jenkins* et al., 2010]. We propose Williams Ice Stream, therefore, as an analogous setting with potential for significant future retreat once the coastal pinning point is breached. This hypothesis calls for much improved knowledge of the subglacial geometry of the GL at Williams Ice Stream/Venable Ice Shelf as an important scientific objective to facilitate numerical modelling of the region's future.

5. Conclusions

Our analysis of Landsat-derived grounding line change reveals that ~65% of the grounding line of the Bellingshausen Sea margin retreated between 1990 and 2015. The changes are pronounced, as expected, in locations where known bathymetric lows across the continental shelf facilitate ocean-driven dynamic thinning (e.g. Ferrigno Ice Stream), but have occurred

more pervasively along the entire coastline than has previously been reported, implicating the likely ingress of relatively warm circumpolar deep water to the majority of the Bellingshausen Sea margin. Nevertheless, despite extensive thinning over recent decades, we observe only minimal grounding line retreat at Venable Ice Shelf. Hypothesized to be currently pinned to a sub-ice topographic high, future sustained shelf thinning at or exceeding recently reported rates would breach this barrier and facilitate ice retreat into a significant inland basin, analogous to nearby Pine Island Glacier. Together, these findings warrant the requirement for continued observation of this important and dynamically evolving region of Antarctica.

Acknowledgements and Data

FDWC was funded by a Carnegie Trust for the Universities of Scotland Carnegie-Caledonian Ph.D. Scholarship with RGB, hosted in the Edinburgh E3 U.K. Natural Environment Research Council Doctoral Training Partnership and the Scottish Alliance for Geoscience, Society and Environment Graduate School. NG was funded under the European Space Agency's Support to Science Elements CryoSat+ CryoTop study. Landsat data used in this study are available from the USGS/NASA at earthexplorer.usgs.gov/; SAR and Cryosat-2 data are available from the European Space Agency; IceBridge data were acquired as part of NASA's Operation IceBridge Project, and is available at: nsidc.org/icebridge/portal/. FDWC also acknowledges Geosoft Inc. for their contribution of Oasis Montaj & Geophysics licenses used to process gravity data. The authors declare no real or perceived conflicts of interests as a result of this paper. Supplementary data supporting the results of this paper are available in the accompanying supporting information file.

References

Bindschadler, R., et al. (2011), Getting around Antarctica: New high- resolution mappings of the grounded and freely-floating boundaries of the Antarctic Ice Sheet created for the International Polar Year, *Cryosphere*, *5*, 569-588, http://dx.doi.org/10.5194/tcd-5-183-2011.

Bingham, R.G., F. Ferraccioli, E.C. King, R.D. Larter, H.D. Pritchard, A.M. Smith, and D.G., and Vaughan (2012), Inland thinning of West Antarctic Ice Sheet steered along subglacial rifts, *Nature*, *487*, 468-471, doi:10.1038/nature11292.

Brunt, K., H.A. Fricker, L. Padman, T. Scambos, and S. O'Neel (2010), Mapping the grounding zone of the Ross Ice Shelf, Antarctica, ICESat laser altimetry, *Ann. Glaciol.*, *51*, 71–79, doi:10.3189/172756410791392790.

Brunt, K.M., H.A. Fricker, and L. Padman (2011), Analysis of ice plains of the Filchner-Ronne Ice Shelf, Antarctica, using ICESat laser altimetry, *J. Glaciol*, *57(205)*, 965-975.

Cochran, J. R. and R. E. Bell (2010, updated 2014), *IceBridge Sander AIRGrav L1B Geolocated Free Air Gravity Anomalies*, digital media [subset IGGRV1B_20121025_11594800_V016], Boulder, Colorado USA: NASA National Snow and Ice Data Center Distributed Active Archive Center. http://dx.doi.org/10.5067/R1RQ6NRIJV89.

Cochran, J.R., S.S. Jacobs, K.J. Tinto, and R.E. Bell (2014), Bathymetric and oceanic controls on Abbot Ice Shelf thickness and stability, *Cryosphere*, *8*, 877-889, doi:10.5194/tc-8-877-2014.

Corr, H.F.J., C.S.M. Doake, A. Jenkins, and D.G. Vaughan (2001), Investigations of an "ice plain" in the mouth of Pine Island Glacier, Antarctica, *J. Glaciol.*, *47(156)*, 51-57, doi:10.3189/172756501781832395.

Favier, L., G. Durand, S.L. Cornford, G.H Gudmundsson, O. Gagliardini, F. Gillet-Chaulet, T. Zwinger, A.J. Payne, and A.M. Le Brocq (2014), Retreat of Pine Island Glacier controlled by marine ice-sheet instability, *Nat. Clim. Chang.*, *4*, 117-121, doi:10.1038/nclimate2094.

Ferrigno, J.G., A.J. Cook, A.M. Mathie, R.S. Williams, Jr., C. Swithinbank, K.M. Foley, A.J. Fox, J.W. Thomson, and J. Sievers (2009), Coastal-Change and Glaciological Map of the Palmer Land Area, Antarctica: 1947–2009 and accompanying explanatory pamphlet, US Geological Survey, USA, *Geologic Investigations Series Map I–2600–C*.

Fretwell, P., et al. (2013), Bedmap2: Improved ice bed, surface and thickness datasets for Antarctica, *Cryosphere*, *7*, 375–393, doi:10.5194/tc-7-375-2013.

Fricker, H.A., Coleman, R., Padman, L., Scambos, T.A., Bohlander, J. and Brunt, K.M (2009), Mapping the grounding zone of the Amery Ice 422 Shelf, East Antarctica using DInSAR, MODIS and ICESat, *Antarct. Sci.*, *21(5)*, 515–532, doi: 10.1017/S095410200999023X.

Fricker, H.A. and L. Padman (2006), Ice shelf grounding zone structure from ICESat laser altimetry, *Geophys. Res. Lett.*, *33(15)*, L15502, doi:10.1029/2006GL026907.

Goldberg, D.N., P. Heimbach, I. Joughin, and B. Smith (2015), Committed retreat of Smith, Pope, and Kohler Glaciers over the next 30 years inferred by transient model calibration, *Cryosphere*, *9*, 2429-2446, doi:10.5194/tc-9-2429-2015.

Graham, A.G.C., R.D. Larter, and F.O. Nitsche (2011), An improved bathymetry compilation for the Bellingshausen Sea, Antarctica, to inform ice sheet and ocean models, *Cryosphere, 5,* 95-106, doi:10.5194/tc-5-95-2011.

Gray, L., D. Burgess, L. Copland, R. Cullen, N. Galin, R. Hawley, and V. Helm (2013), Interferometric swath processing of CryoSat-2 data for glacial ice topography, *Cryosphere*, *7,* 1857-1867.

Haran, T., J. Bohlander, T. Scambos, T. Painter, and M. Fahnestock (2005, updated 2013), *MODIS Mosaic of Antarctica 2003-2004 (MOA2004) Image Map, digital media,* Boulder, Colorado, USA: National Snow and Ice Data Center. http://dx.doi.org/10.7265/N5ZK5DM5.

Haran, T., J. Bohlander, T. Scambos, T. Painter, and M. Fahnestock (2014), *MODIS Mosaic of Antarctica 2008-2009 (MOA2009) Image Map*, digital media, Boulder, Colorado, USA: National Snow and Ice Data Center. http://dx.doi.org/10.7265/N5KP8037.

Hawley, R. L., A. Shepherd, R. Cullen, V. Helm, and D. J. Wingham (2009), Ice-sheet elevations from across-track processing of airborne interferometric radar altimetry, *Geophys. Res. Lett*., *36,* L22501.

Holt, T.O., H.A. Fricker, N.F. Glasser, O. King, A. Luckman, L. Padman, D.J Quincey, and M.R. Siegfried (2014), The structural and dynamic responses of Stange Ice Shelf to recent environmental change, *Antarct. Sci., 26(6),* 646-660, doi:10.1017/S095410201400039X.

Jenkins, A., et al. (2010), Observations beneath Pine Island Glacier in West Antarctica and implications for its retreat, *Nat. Geosci., 3(7),* 468–472, doi:10.1038/ngeo890.

Jacobs, S.S., A. Jenkins, CF. Giulivi and P. Dutrieux (2011), Stronger ocean circulation and increased melting under Pine Island Glacier ice shelf, *Nat. Geosci., 4*, 519-523, doi:10.1038/ngeo1188.

Joughin, I., R.B. Alley, and D.M. Holland (2012), Ice-Sheet Response to Oceanic Forcing, *Science, 38*, 1172-1176, doi:10.1126/science.1226481.

Joughin, I., B.E. Smith, and B. Medley (2014) Marine ice sheet collapse potentially under way for the Thwaites Glacier basin, West Antarctica, *Science, 344(6185)*, 735-738, doi: 10.1126/science.1249055.

Lee, D.S., J.C. Storey, M.J. Choate, and R.W. Hayes (2004), Four Years of Landsat-7 On-Orbit Geometric Calibration and Performance, *IEEE Trans. Geosci. Remote Sens., 42(12)*, 2786-2795, doi:10.1109/TGRS.2004.836769.

Lenaerts, J.T.M., M.R. van den Broeke, W.J. van de Berg, E. van Meijgaard, and P. Kuipers Menneke (2012) A new, high-resolution surface mass balance map of Antarctica (1979-2010) based on regional atmospheric climate modelling, *Geophys. Res. Lett., 39(4)*, GL050713, doi: 10.1029/2011GL050713.

Leuschen, C., P. Gogineni, F. Rodriguez-Morales, J. Paden, and C. Allen (2010a, updated 2015a), *IceBridge MCoRDS L2 Ice Thickness, Version 1, digital media* [subset IRMCR_20091103_02], Boulder, Colorado, USA. NASA National Snow and Ice Data Center Distributed Active Archive Center. http://dx.doi.org/10.5067/GDQ0CUCVTE2Q.

Leuschen, C., P. Gogineni, F. Rodriguez-Morales, J. Paden, and C. Allen (2010b, updated 2015b), *IceBridge MCoRDS L2 Ice Thickness, Version 1, digital media* [subset IRMCR2_20111116_02], Boulder, Colorado, USA. NASA National Snow and Ice

Data Center Distributed Active Archive Center. http://dx.doi.org/10.5067/GDQ0CUCVTE2Q.

MacGregor, J.A., G.A. Catania, M.S. Markowski and A.G. Andrews (2012), Widespread rifting and retreat of ice-shelf margins in the eastern Amundsen Sea Embayment between 1972 and 2011, *J. Glaciol*, *58(209)*, 458-466, doi: 10.3189/2012JoG11J262.

McMillan, M., A. Shepherd, A. Sundal, K. Briggs, A. Muir, A. Ridout, A. Hogg, and D. Wingham (2014), Increased ice losses from Antarctica detected by CryoSat-2, *Geophys. Res. Lett.*, *41(11)*, 3988-3905, doi:10.1002/2014GL060111.

Ó Cofaigh, C.O., J.A. Dowdeswell, J. Evans, C-D. Hillenbrand, R.D. Larter, P. Morris, and C.J. Pudsey (2005), Flow of the West Antarctic Ice Sheet on the continental margin of the Bellingshausen Sea at the Last Glacial Maximum, *J. Geophys. Res.*, *110*, b11103, doi:10.1029/2005jb003619.

Paolo, F.S., H.A. Fricker, and L. Padman (2015), Volume loss from Antarctic ice shelves is accelerating, *Science*, *348*, 327-331, doi:10.1126/science.aaa0940.

Park, J. W., N. Gourmelen, A. Shepherd, S. W. Kim, A. Vaughan, and D. G. Wingham (2013), Sustained retreat of the Pine Island Glacier, *Geophys. Res. Lett.*, *40*, 2137–2142, doi:10.1002/grl.50379.

Pritchard, H. D., R. J. Arthern, D. G. Vaughan, and L. A. Edwards (2009), Extensive dynamic thinning on the margins of the Greenland and Antarctic ice sheets, *Nature*, *461*, 971–975, doi:10.1038/nature08471.

Pritchard, H.D., S.R.M. Ligtenberg, H.A. Fricker, D.G. Vaughan, M.R. van den Broeke, and L. Padman (2012), Antarctic ice sheet loss driven by basal melting of ice sheets, *Nature*, *484*, 502-505, doi:10.1038/nature10968.

Rignot, E., J. L. Bamber, M. R. van den Broeke, C. Davis, Y. Li, W. J. van de Berg, and E. van Meijgaard (2008), Recent Antarctic ice mass loss from radar interferometry and regional climate modelling, *Nat. Geosci.*, *1*, 106–110, doi:10.1038/ngeo102.

Rignot, E., J. Mouginot, and B. Scheuchl (2011), Antarctic grounding line mapping from differential satellite radar interferometry, *Geophys. Res. Lett.*, *38*, L10504, doi:10.1029/2011GL047109.

Rignot, E., J. Mouginot, M. Morlighem, H. Seroussi, and B. Scheuchl (2014), Widespread, rapid grounding line retreat of Pine Island, Thwaites, Smith, and Kohler glaciers, West Antarctica, from 1992 to 2011, *Geophys. Res. Lett.*, *421(10)*, 3502-3509, doi: 10.1002/2014GL060140.

Scambos, T.A., T.M. Haran, M.A. Fahnestock, T.H. Painter, and J. Bohlander (2007), MODIS-based Mosaic of Antarctica (MOA) data sets: Continent-wide surface morphology and snow grain size, *Remote Sens. Environ.*, *111*, 242–257, doi:10.1016/j.rse.2006.12.020.

Scott, J.B.T., G.H. Gudmundsson, A.M. Smith, R.G. Bingham, H.D. Pritchard, and D.G. Vaughan (2009), Increased rate of acceleration on Pine Island Glacier strongly coupled to changes in gravitational driving stress, *Cryosphere*, *3*, 125-131, doi: 10.5194/tc-3-125-2009.

Seroussi. H., M. Morlighem, E. Rignot, J. Mouginot, E. Larour, M. Schodlok, and A. Khazendar (2014), Sensitivity of the dynamics of Pine Island Glacier, West Antarctica, to climate forcing for the next 50 years, *Cryosphere*, *8*, 1699-1710, doi:10.5194/tc-8-1699-2014.

Shepherd, A., D. Wingham, and E. Rignot (2004), Warm ocean is eroding West Antarctic Ice Sheet, *Geophys. Res. Lett.*, *31(23)*, L23402, doi:10.1029/2004GL021106.

Shepherd, A., D. Wingham, D. Wallis, K. Giles, S. Laxon, and A.V. Sundal (2010), Recent loss of floating ice and the consequent sea level contribution, *Geophys. Res. Lett.*, *37(13)*, L13503, doi:10.1029/2010GL042496.

Shepherd, A. et al. (2012), A Reconciled Estimate of Ice-Sheet Mass Balance, *Science*, *338(6111)*, 1183-1189, doi:10.1126/science.1228102.

Storey, J., M. Choate, and K. Lee (2014), Landsat 8 Operational Land Imager On-Orbit Geometric Calibration and Performance, *Remote Sens.*, *6(11)*, 11127-11152, doi: 10.3390/rs61111127.

Swithinbank, C., R.S. Williams, Jr., J.G. Ferrigno, K.M. Foley, C.E. Rosanova, and L.M. Dailide (2004), Coastal-change and glaciological map of the Eights coast area, Antarctica: 1972–2001 and accompanying explanatory pamphlet, US Geological Survey, USA, *Geologic Investigations Series Map I–2600–E*.

Tucker, C.J., D.M. Grant, and J.D. Dykstra, (2004), NASA's Global Orthorectified Landsat Data Set Compton, *Photogramm. Eng. Remote Sens.*, *70(3)*, 313-322, doi: 10.14358/PERS.70.3.313.

Vaughan, D.G., J.C. Comiso, I. Allison, J. Carrasco, G. Kaser, R. Kwok, P. Mote, T. Murray, F. Paul, J. Ren, E. Rignot, O. Solomina, K. Steffen, and T. Zhang (2013), Observations: Cryosphere, In: *Climate Change 2013: The Physical Science Basis. Contribution of Working Group I to the Fifth Assessment Report of the Intergovernmental Panel on Climate Change*, 317-382, Cambridge University Press, Cambridge, United Kingdom and New York, NY, USA.

Walker, D.P., M.A., Brandon, A. Jenkins, J.T., Allen, J.A. Dowdeswell, and J. Evans (2007), Oceanic heat transport onto the Amundsen Sea shelf through a submarine glacial trough, *Geophys. Res. Lett.*, *34*, L02602, 1-4, doi:10.1029/2006GL028154.

Williams, C.R., R.C.A. Hindmarsh, and R.J. Arthern (2014), Calculating balance velocities with a membrane stress correction, *J. Glaciol.*, *60(220)*, 294-304, doi: 10.3189/2014JoG13J092.

Wouters, B., A. Martin-Español, V. Helm, T. Flament, J. M. van Wessem, S. R. M. Ligtenberg, M. R. van den Broeke, and J. L. Bamber (2015), Dynamic thinning of glaciers on the Southern Antarctic Peninsula, *Science*, *348*, 899-903, doi:10.1126/science.aaa5727.

Figure Captions

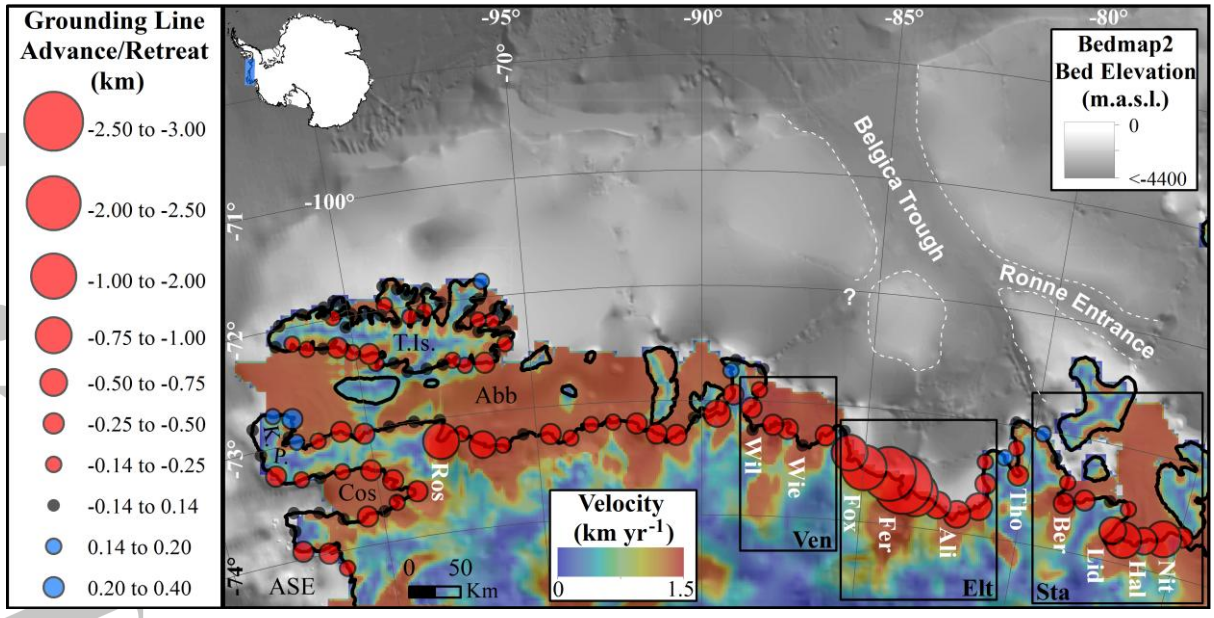

Figure 1. Net grounding line (GL) change along Bellingshausen Sea coastline of West Antarctica between 1990 and 2015 derived from Landsat mapping of I_b. Circle radii denote the magnitude and direction of change (red: *retreat*, blue: *advance*) for every 30 km segment of the BSS GL. Note the non-linear scaling of change. Small black circles symbolise negligible detectable change within Landsat error bounds (cf. Table S2). Change symbols are superimposed over modelled depth-averaged ice velocity [km yr^{-1}; *Williams* et al., 2014] and continental shelf bathymetry [*Fretwell* et al., 2013]. Inset (top left): study location. Thin broken white lines delineate the dimensions of the Belgica Trough; the Ronne Entrance tributary trough; and the area of deep bathymetry which potentially connects the margin of the Venable Ice Shelf to Belgica Trough. *Sta* and *Ven* denote the *Stange* and *Venable Ice Shelves* (respectively); *Elt*, *Eltanin Bay*; *T.Is.*, Thurston Island; *Abb*, Abbot Ice Shelf; *Cos*, Cosgrove Ice Shelf; *K.P.*, King Peninsula; *ASE*, Amundsen Sea Embayment; *Nik*, Nikitin Glacier; *Hal*, Hall Glacier; *Lid*, Lidke Ice Stream; *Ber*, Berg Ice Stream; *Tho*, Thompson Glacier; *Ali*, Alison Ice Stream; *Fer*, Ferrigno Ice Stream; *Fox*, Fox Ice Stream; *Wie*, Wiesnet Ice Stream; *Wil*, Williams Ice Stream; *Ros*, Rosanova Glacier.

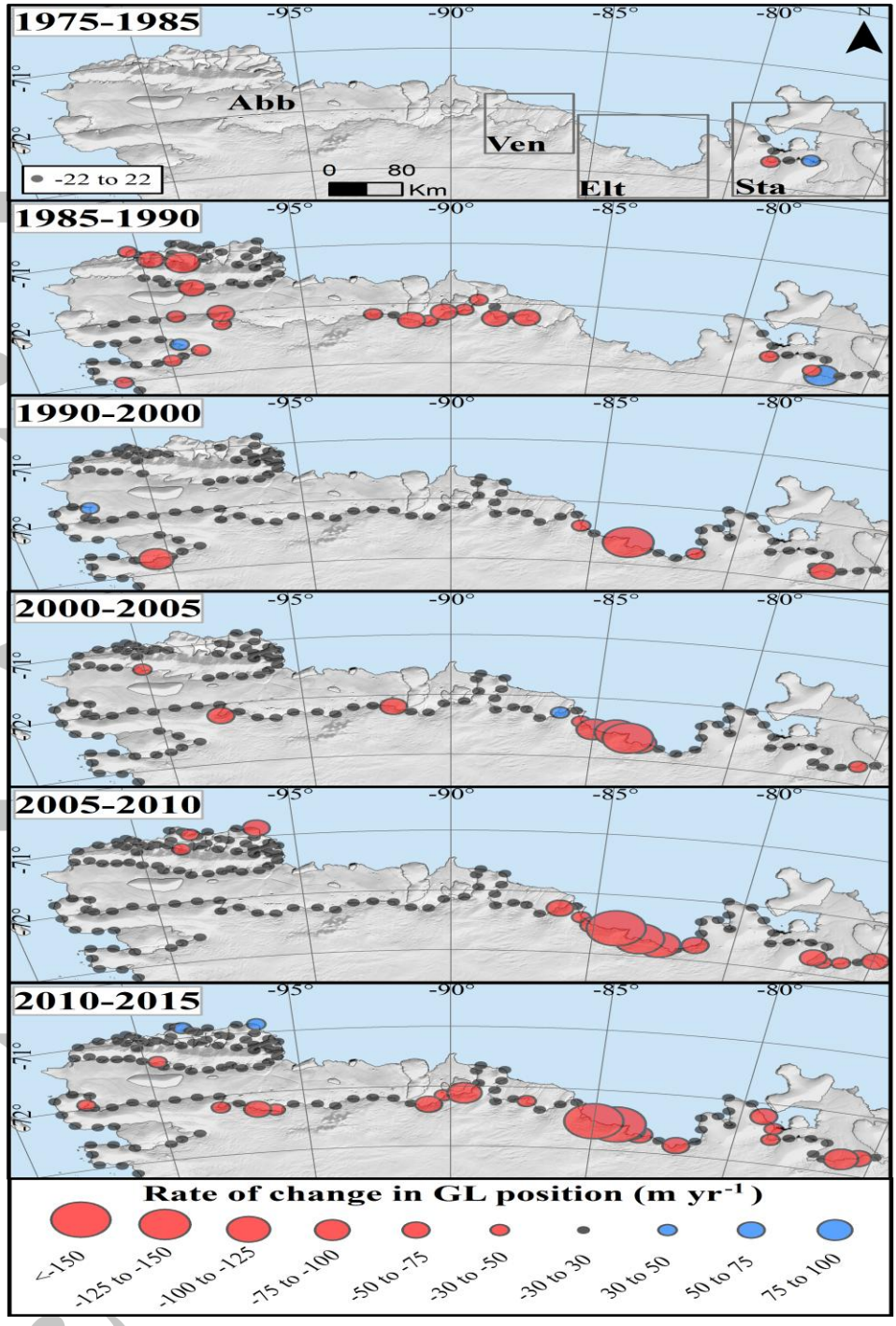

Figure 2. Rate of change in GL position over 5-10 year epochs between 1975 and 2015. Circle radii denote the magnitude and direction of change (red: *retreat*, blue: *advance*) for every 30 km segment; black circles indicate changes within Landsat error bounds. Note the non-linear scaling of change, and different scale for 1975-1985 error bounds. Site labels as per Figure 1. Data overlaid upon MOA2004 [Haran et al., 2013].

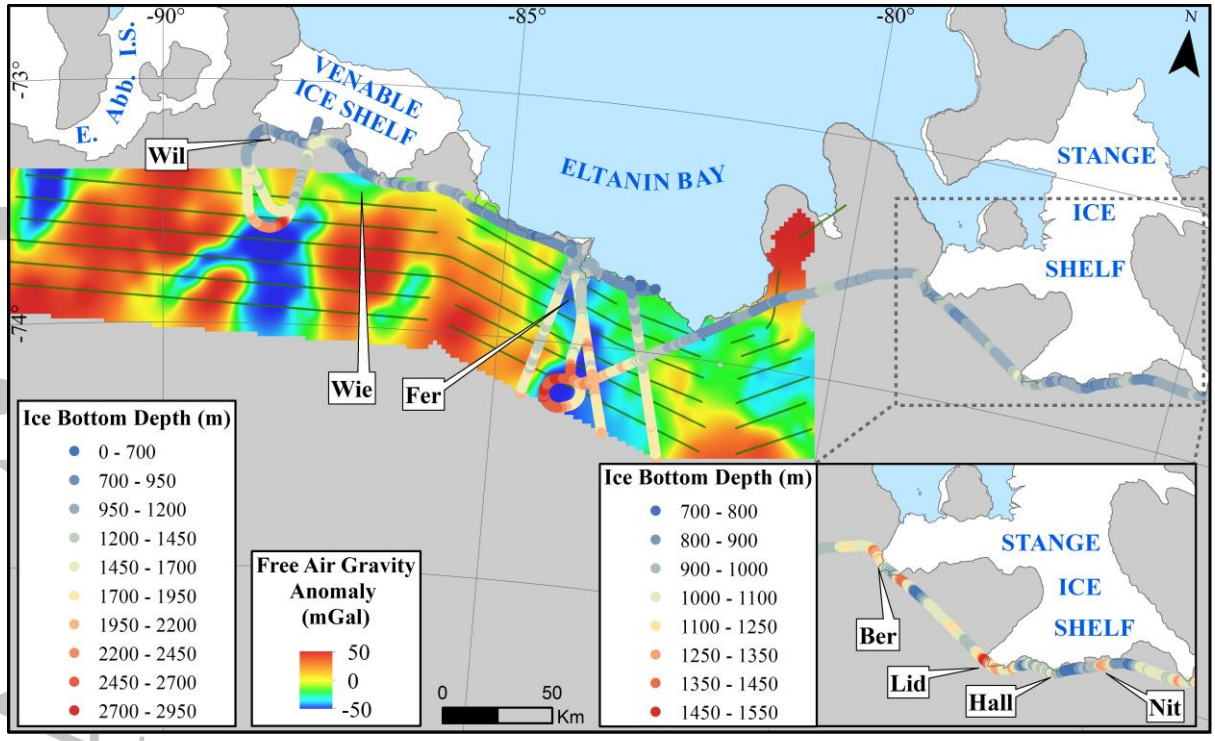

Figure 3. IceBridge radar and gridded free-air gravity anomaly data over the eastern BSS. Radar profiles were acquired on 3 November 2009 and 16 November 2011 [*Leuschen* et al., 2015a, 2015b]; gravity data were acquired on 25 October 2012 (flight-lines in green) [*Cochran & Bell*, 2014]. *E. Abb. I.S.* denotes eastern Abbot Ice Shelf. Inset shows enlarged radar-derived ice bottom depths at Stange Ice Shelf. All other site labels as per Figure 1. Black lines delineate the 2008/2009 MOA GL [*Haran* et al., 2014].

Geophysical Research Letters

Supporting Information for

Four-decade record of pervasive grounding line retreat along the Bellingshausen margin of West Antarctica

Frazer D.W. Christie[1], Robert G. Bingham[1], Noel Gourmelen[1] Simon F.B. Tett[1], Atsuhiro Muto[2]

[1]School of GeoSciences, University of Edinburgh, Drummond Street, Edinburgh, EH8 9XP

[2]Department of Earth and Environmental Science, Temple University, USA

Contents of this file

Additional Supporting Information (Files uploaded separately)

Dataset S1
Tables S1 and S4

Introduction

This file contains additional information pertaining to the derivation, analysis and interpretation of the results presented in this study. Landsat, ERS-1/2 Synthetic Aperture Radar (SAR), Operation IceBridge and CryoSat-2 data were acquired between 2013 and 2016 from publically available NASA and ESA data repositories. MODIS MOA and Bedmap2 data products were obtained from the NSIDC data portal and the SCAR Antarctic Digital Database, respectively. Detection of grounding line (GL) change was completed using standard GIS software and SAR processing was carried out using commercial Interferometric Synthetic Aperture Radar (InSAR) processing tools. At time of publication, the authors declare no known imperfections or anomalies within the data sets.

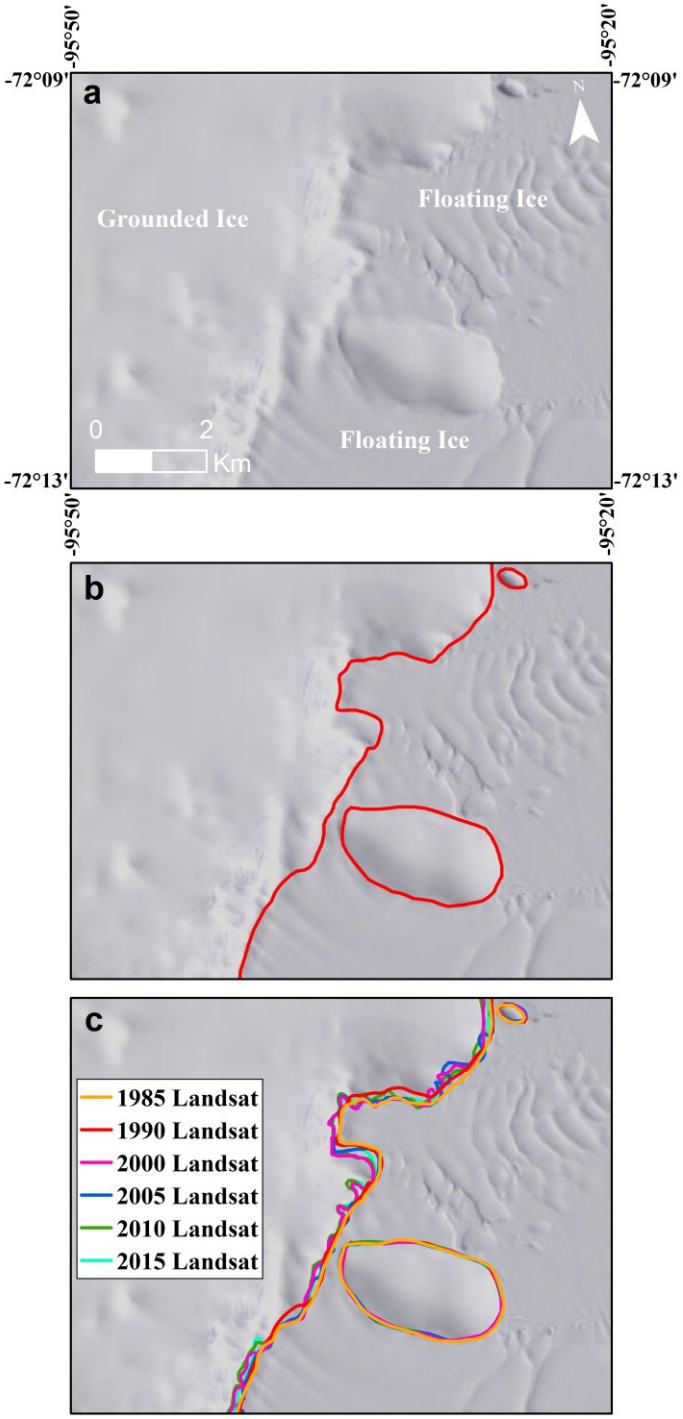

Figure S1. Visual summary of break-in-slope mapping. ***a***, Landsat scene acquired on 20 February 1991. Image shows a clearly identifiable break-in-slope between the grounded ice (eastern Thurston Island) and adjacent, floating ice. Two grounded ice rises are also visible. ***b***, The break-in-slope is digitized for year c.1990, and represents Point I_b. ***c***, This process was carried out along the whole BSS and was repeated for all other epochs, using Landsat imagery acquired during 1975 (not available in this location hence not depicted in the example above), c.1985, 2000, 2005, 2010 and 2015.

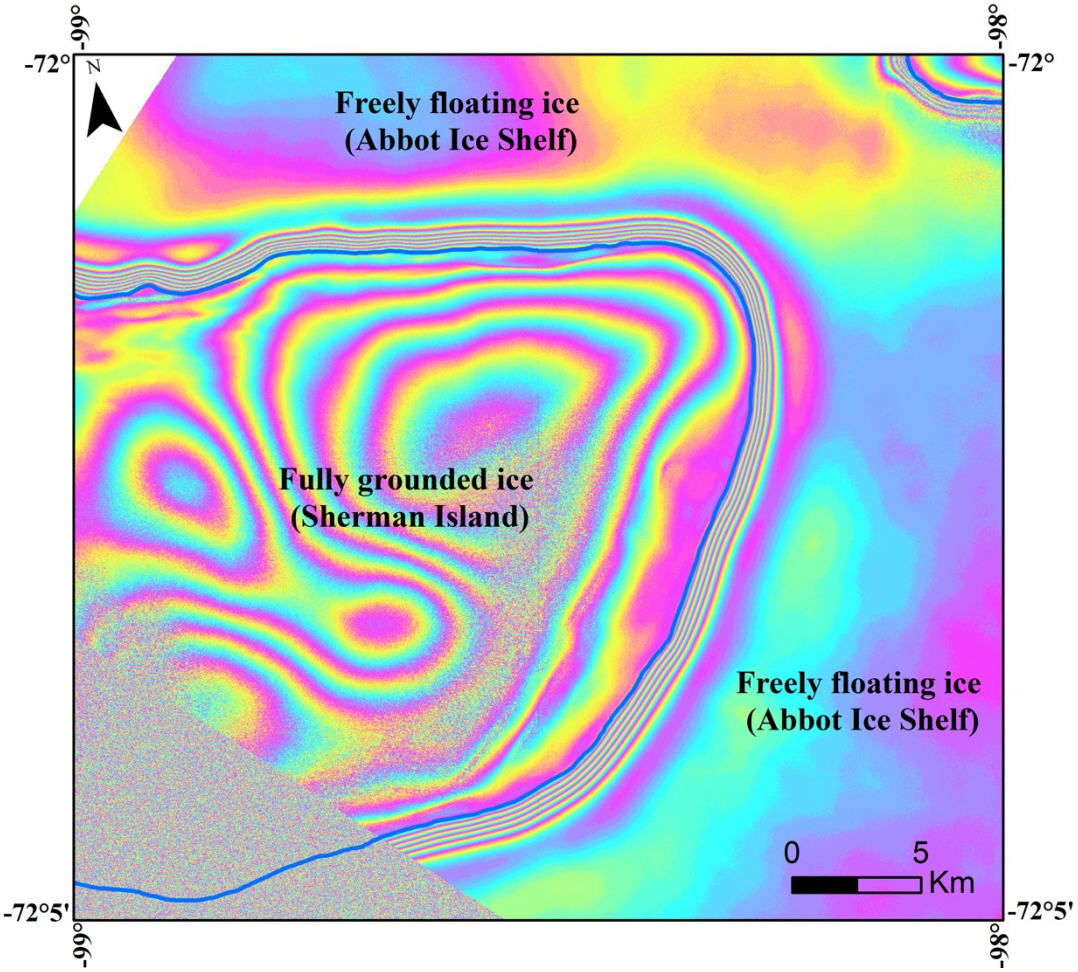

Figure S2. Double differential interferogram showing Abbot Ice Shelf and eastern Sherman Island, processed using SAR imagery acquired on 19920123-19920126 and 19920129-19920201 (3-day temporal baseline). The absolute limit of tidal flexure (*F*; blue line) is delineated by the landward limit of closely-spaced fringes observed between the freely-floating ice shelf and fully-grounded ice [cf. *Fricker* et al., 2009; their Figure 2].

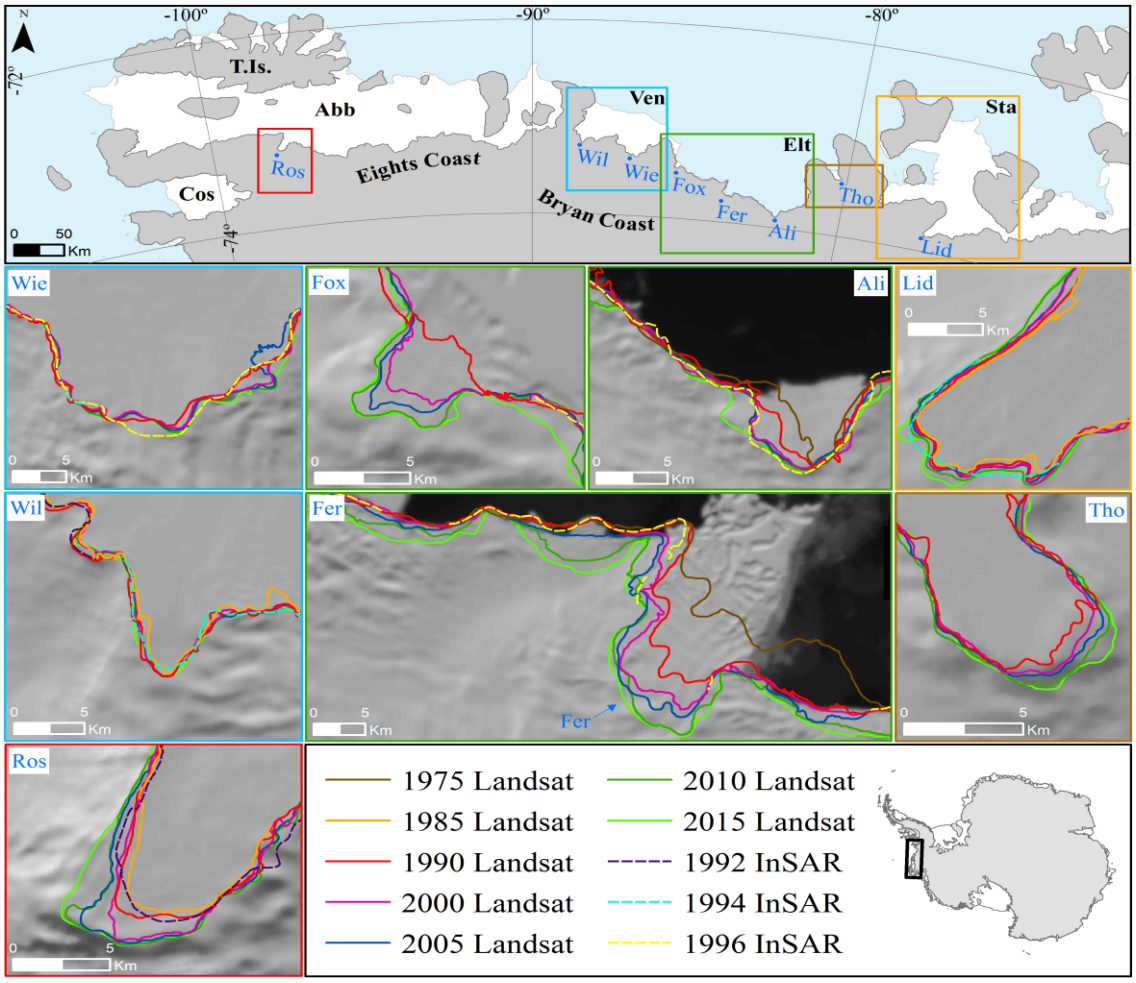

Figure S3. Examples of I_b migration and comparison with InSAR-derived F at selected locations in the BSS. Boxes in top panel are color-coded to correspond with matching color-bordered inset panels. Labelled sites as per Figure 1. 1975/1985 I_b lines are absent in some panels due to the lack of Landsat spatial coverage during these epochs. Top panel is superimposed on the MOA2004 continental outline [*Haran* et al., 2013], and black lines delineate the 2008/2009 MOA GL [*Haran* et al., 2014]. All other panels are superimposed over MOA2004 [*Haran* et al., 2013]. Inset (bottom right): study location.

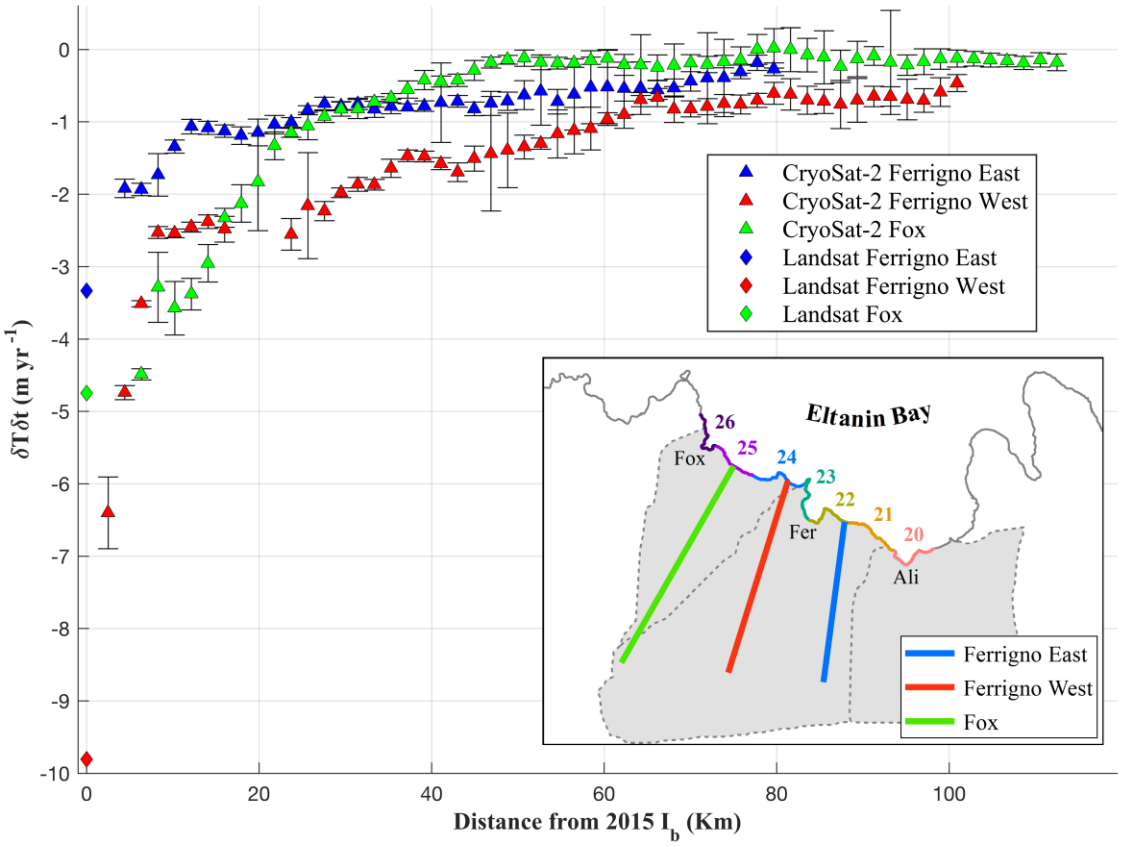

Figure S4. Rates of thickness change (δT/δt) over selected profiles in Eltanin Bay, derived from CryoSat-2 observations and Landsat-derived GL thinning estimations for the period 2010-2015 (refer to Text S3 for more information on estimating Landsat and CryoSat-2 thinning rates). Inset shows Eltanin Bay and locations of profiles shown in graph. Fox, Ferrigno and Alison Ice Stream drainage catchments shown in gray. Colored GLs and corresponding numbers refer to selected 30 km segment sites within the Eltanin Bay region, as discussed in main text and Data Set S1.

Text S1. Quantification of Landsat positional accuracy

Following *Bindschadler* et al. [2011], error in the mapping of Point I_b is dependent on the nature of the grounded-ice boundary and the geometric error associated with each Landsat satellite platform (i.e. the orbital/geo-positional error associated with successive Landsat passes; cf. *USGS* [2015]), assuming tidal variation in the position of the grounding zone to be negligible. Hence, where the boundary transition is from grounded ice to open ocean, we mapped I_b to within one Landsat scene pixel (i.e. a prescribed one pixel error; where pixel value is dictated by the spatial resolution of the satellite sensor used (Table S2)). For grounded-ice/sea-ice transitions, where the boundary is potentially more ambiguous, we mapped to within two Landsat pixels of error. At the deeply bedded Ferrigno Ice Stream, where ice velocities exceed 1 km yr^{-1} [*Rignot* et al., 2008; *Williams* et al., 2014] and the break in slope is more ambiguously located compared to neighboring (more steeply bedded) locations, we assigned a 500 m error boundary in accordance with Bindschadler et al. [2011]. Along the remaining boundaries of the BSS coastline, we prescribed a three-pixel error. These include regions of slow-flowing grounded ice flowing into ice shelves and some outlet glaciers where I_b is more readily identifiable than faster flowing ice streams.

Accordingly, following the discussion in *Bindschadler* et al. [2011], estimations of positional error (1σ) were calculated as the root-sum-square of I_b delineation accuracy and satellite geometric error. These create the positional accuracy estimations found in Table S2.

In order to propagate error between successive I_b observations (e.g. the results shown in Figure 1), we calculated the root-sum-square of the (1σ) positional errors associated with Landsat 8 (i.e. for the 2015 baseline, refer to main text Section 2.3) and the earlier Landsat platform under analysis for a given epoch. Thus, for example, in Figure 1, the majority of accumulative errors in the BSS equal 137 m, as the grounding line boundary type is classed as 'Slow-ice-to Shelf or Outlet Glacier' (Table S2; e.g. $\sqrt[2]{91^2 + 103^2}$). For Figure 2, scaled error approximations were derived by dividing these errors by the temporal period under question.

Text S2. I_b change quantification: Calculation of 5- to 10-year change.

Following completion of the I_b change calculations detailed in the main text (section 2.3), changes in I_b position over 5- to 10-year periods were calculated using the following expression:

$$\frac{\delta I_b}{\delta t} = \frac{\delta I_{b\,[2015-y0]} - \delta I_{b\,[2015-y+1]}}{\delta t} \quad [1]$$

where $\delta I_b/\delta t$ corresponds to the change in I_b per 30-km segment over 5- to 10-year period; $\delta I_{b[2015\text{-}y0]}$ is the change in I_b over the earliest epoch under examination (e.g. change in 2005 GL to the baseline 2015 GL); $\delta I_{b[2015\text{-}y+1]}$ is the change in I_b over the immediately succeeding epoch (e.g. 2010 to 2015); and δt is the temporal period between the two epochs. Refer to Data Set S1 and Figure 2 for raw data and examples of this process.

Notably, owing to the limited spatial and/or temporal availability of Landsat imagery across some regions of the BSS (especially for 1975), the above processes were not carried out in sectors containing no [2015-*y*] data for one or both epochs under analysis.

Text S3. CryoSat-2-derived elevation change for ice draining into Eltanin Bay, and comparisons with 2010-2015 Landsat-derived estimations of ice thinning at the GL.

Rates of surface elevation change were generated from swath processing of CryoSat-2 data acquired between 2010 and 2015. Swath processing is enabled by the Synthetic Aperture Radar Interferometric (SARIn) mode of CryoSat-2 and enables one to two orders of magnitude more elevation measurements than conventional point-of-closest-approach (hereafter POCA) altimetry techniques, thereby allowing increased spatial and temporal resolution and improved coverage of ice-sheet marginal areas [*Hawley* et al. 2009; *Gray* et al. 2013]. Linear rates of surface elevation change were then derived at 500 m posting using a repeat track approach [*McMillan* et al., 2014]. Across Eltanin Bay, where we detect the greatest changes in GL position over the observational period 2010-2015, we extracted 3 profiles across the Ferrigno and Fox catchment regions (Figure S4). These profiles reveal increasing trends of rates of surface elevation change ($\delta T/\delta t$) towards the GL, with maximum values occurring at Ferrigno West (-6.40 m yr^{-1}, $\sigma = \pm 0.49$ m yr^{-1}; Figure S4). Notably, average $\delta T/\delta t$ across all 3 profiles equals -0.84 m yr^{-1} ($\sigma = \pm 0.21$ m yr^{-1}), which compares well with previously reported CryoSat-2 POCA observations in this area [*McMillan* et al., 2014; *Wouters* et al., 2015].

In addition to CryoSat-2-derived $\delta T/\delta t$, theoretical thinning rates over the same epoch (2010-2015) were calculated using our Landsat-derived observations of I_b change. Rates were calculated using the empirical formula detailed in *Park* et al. [2013], whereby theoretical $\delta T/\delta t$ is a function of GL retreat, surface topography/slope, subglacial bed topography/slope, seawater density (1027.5 kg m^{-3}) and the density of ice (917 kg m^{-3}). Our calculations utilized surface and bed slopes inferred from BEDMAP2 [*Fretwell* et al., 2013], and produced the theoretical estimations shown in Figure S4.

Overall, our estimations show excellent agreement with CryoSat-2 swath observations at Ferrigno East and Fox, indicating increasing trends of negative $\delta T/\delta t$ towards the GL at these locations. The high Landsat-derived $\delta T/\delta t$ value calculated for Ferrigno West (-9.8 m yr^{-1}) is believed to be subject to error, associated with the dramatic break up of ice and corresponding GL retreat across this sector between 2010 and 2015 (Figure 2; Figure S3). Nonetheless, the close agreement between Landsat and CryoSat-2 thinning values at Ferrigno East and Fox supplements other independent observations of dynamic thinning across the Eltanin Bay region in recent years [*Rignot* et al., 2008; *Bingham* et al., 2012; *McMillan* et al., 2014, *Wouters* et al., 2015], and acts as auxiliary validation of our Landsat I_b mapping.

Table S1. Landsat data used in the present study.

(File uploaded separately as 2016GL068972-ts01.pdf)

Platform	*Year Mapped*	*Grounded Ice Boundary Classification*	*Spatial Resolution (m)*	*Prescribed Pixel Error (m)*	*Geometric Error[1] (m)*	*Positional Error (1σ; m)*
Landsat 2 (MSS[2])	1975	Open ocean	60	1 (60)	<100	117
		Grounded-ice/Sea-ice		2 (120)		156
		Slow-ice-to Shelf or Outlet Glacier		3 (180)		206
		Fast flowing, deeply bedded grounded ice		500		510
Landsat 4,5 (TM[3]), 7 (ETM+[4])	1985 1990 2000 2005 2010	Open ocean	30	1 (30)	<50	58
		Grounded-ice/Sea-ice		2 (60)		78
		Slow-ice-to Shelf or Outlet Glacier		3 (90)		103
		Fast flowing, deeply bedded grounded ice		500		502
Landsat 8 (OLI[5])	2015	Open ocean	30	1 (30)	12	32
		Grounded-ice/Sea-ice		2 (60)		61
		Slow-ice-to Shelf or Outlet Glacier		3 (90)		91
		Fast flowing, deeply bedded grounded ice		500		500

[1]Geometric error values derived from *Lee* et al. [2004]; *Tucker* et al. [2004], *Bindschadler* et al. [2011], *Storey* et al. [2014]. [2]*Multispectral Scanner*. [3]*Thematic Mapper*. [4]*Enhanced Thematic Mapper Plus*. [4]*Operational Land Imager*

Table S2. Landsat platform-specific positional accuracy (1σ) estimations for BSS grounded ice boundary classifications.

Table S3. ERS-1/2 Synthetic Aperture Radar imagery used to make double-differential interferograms.

(File uploaded separately as 2016GL068972-ts03.pdf)

Data Set S1. GL change values generated in this study.

File uploaded separately as 2016GL068972-ds01.xslx

References

Bindschadler, R., et al. (2011), Getting around Antarctica: New high- resolution mappings of the grounded and freely-floating boundaries of the Antarctic Ice Sheet created for the International Polar Year, *Cryosphere*, *5*, 569-588, http://dx.doi.org/10.5194/tcd-5-183-2011.

Bingham, R.G., F. Ferraccioli, E.C. King, R.D. Larter, H.D. Pritchard, A.M. Smith, and D.G., and Vaughan (2012), Inland thinning of West Antarctic Ice Sheet steered along subglacial rifts, *Nature*, *487*, 468-471, doi:10.1038/nature11292.

Ferrigno, J.G., A.J. Cook, A.M. Mathie, R.S. Williams, Jr., C. Swithinbank, K.M. Foley, A.J. Fox, J.W. Thomson, and J. Sievers (2009), Coastal-Change and Glaciological Map of the Palmer Land Area, Antarctica: 1947–2009 and accompanying explanatory pamphlet, US Geological Survey, USA, *Geologic Investigations Series Map I–2600–C*.

Fretwell, P., et al. (2013), Bedmap2: Improved ice bed, surface and thickness datasets for Antarctica, *Cryosphere*, *7*, 375–393, doi:10.5194/tc-7-375-2013.

Fricker, H.A., et al. (2009), Mapping the grounding zone of the Amery Ice Shelf, East Antarctica using DInSAR, MODIS and ICESat, *Antarct. Sci.*, *21(5)*, 515–532, doi: 10.1017/S095410200999023X.

Gray, L., D. Burgess, L. Copland, R. Cullen, N. Galin, R. Hawley, and V. Helm (2013), Interferometric swath processing of CryoSat-2 data for glacial ice topography, *The Cryosphere Discussions*, *7*, 3133-31621857-1867.

Haran, T., J. Bohlander, T. Scambos, T. Painter, and M. Fahnestock (2005, updated 2013), *MODIS Mosaic of Antarctica 2003-2004 (MOA2004) Image Map, digital media,* Boulder, Colorado, USA: National Snow and Ice Data Center. http://dx.doi.org/10.7265/N5ZK5DM5.

Haran, T., J. Bohlander, T. Scambos, T. Painter, and M. Fahnestock (2014), *MODIS Mosaic of Antarctica 2008-2009 (MOA2009) Image Map*, digital media, Boulder, Colorado, USA: National Snow and Ice Data Center. http://dx.doi.org/10.7265/N5KP8037.

Hawley, R. L., A. Shepherd, R. Cullen, V. Helm, and D. J. Wingham (2009), Ice-sheet elevations from across-track processing of airborne interferometric radar altimetry, *Geophys. Res. Lett.*, *36*, L22501.

Lee, D.S., J.C. Storey, M.J. Choate, and R.W. Hayes (2004), Four Years of Landsat-7 On-Orbit Geometric Calibration and Performance, *IEEE Trans. Geosci. Remote Sens.*, *42(12)*, 2786-2795, doi:10.1109/TGRS.2004.836769.

Leuschen, C., P. Gogineni, F. Rodriguez-Morales, J. Paden, and C. Allen (2010a, updated 2015a), *IceBridge MCoRDS L2 Ice Thickness, Version 1, digital media* [subset IRMCR_20091103_02], Boulder, Colorado, USA. NASA National Snow and Ice Data Center Distributed Active Archive Center. http://dx.doi.org/10.5067/GDQ0CUCVTE2Q.

Leuschen, C., P. Gogineni, F. Rodriguez-Morales, J. Paden, and C. Allen (2010b, updated 2015b), *IceBridge MCoRDS L2 Ice Thickness, Version 1, digital media* [subset IRMCR2_20111116_02], Boulder, Colorado, USA. NASA National Snow and Ice Data Center Distributed Active Archive Center. http://dx.doi.org/10.5067/GDQ0CUCVTE2Q.

McMillan, M., A. Shepherd, A. Sundal, K. Briggs, A. Muir, A. Ridout, A. Hogg, and D. Wingham (2014), Increased ice losses from Antarctica detected by CryoSat-2, *Geophys. Res. Lett.*, *41(11)*, 3988-3905, doi:10.1002/2014GL060111.

Paolo, F.S., H.A. Fricker, and L. Padman (2015), Volume loss from Antarctic ice shelves is accelerating, *Science*, *348*, 327-331, doi:10.1126/science.aaa0940.

Rignot, E., J. L. Bamber, M. R. van den Broeke, C. Davis, Y. Li, W. J. van de Berg, and E. van Meijgaard (2008), Recent Antarctic ice mass loss from radar interferometry and regional climate modelling, *Nat. Geosci.*, *1*, 106–110, doi:10.1038/ngeo102.

Rignot, E., J. Mouginot, and B. Scheuchl (2011), Antarctic grounding line mapping from differential satellite radar interferometry, *Geophys. Res. Lett.*, *38*, L10504, doi:10.1029/2011GL047109.

Storey, J., M. Choate, and K. Lee (2014), Landsat 8 Operational Land Imager On-Orbit Geometric Calibration and Performance, *Remote Sens.*, *6(11)*, 11127-11152, doi: 10.3390/rs61111127.

Swithinbank, C., R.S. Williams, Jr., J.G. Ferrigno, K.M. Foley, C.E. Rosanova, and L.M. Dailide (2004), Coastal-change and glaciological map of the Eights coast area, Antarctica: 1972–2001 and accompanying explanatory pamphlet, US Geological Survey, USA, *Geologic Investigations Series Map I–2600–E*.

Tucker, C.J., D.M. Grant, and J.D. Dykstra, (2004), NASA's Global Orthorectified Landsat Data Set Compton, *Photogramm. Eng. Remote Sens.*, *70(3)*, 313-322, doi: 10.14358/PERS.70.3.313.

Wouters, B., A. Martin-Español, V. Helm, T. Flament, J. M. van Wessem, S. R. M. Ligtenberg, M. R. van den Broeke, and J. L. Bamber (2015), Dynamic thinning of glaciers on the Southern Antarctic Peninsula, *Science*, *348*, 899-903, doi:10.1126/science.aaa5727.

Year of Acquisition	*Circa Year*	*Day/Month (dd/mm)*	*Satellite Path #*	*Satellite Row #*	*Landsat ID #*
1975	-	18/02	223	111	LM2236111975049AAA06
1975	-	18/02	223	112	LM2236112975049AAA06
1975	-	18/02	223	113	LM2236111975049AAA06
1984	1985	10/12	2	113	LM51511331984345AAA03
1986	1985	21/12	1	111	LT50011121986355XXX05
1986	1985	21/12	1	112	LT50011131986355XXX05
1986	1985	21/12	1	113	LT50011111986355XXX03
1986	1985	21/12	1	114	LT50011141986355XXX05
1986	1985	28/01	217	112	LT52171121986028XXX02
1986	1985	02/02	220	111	LT52201111986033XXX03
1986	1985	02/02	220	112	LT52201121986033XXX03
1986	1985	18/02	220	112	LT52201121986049XXX06
1988	1990	15/12	229	111	LT42291111988350XXX03
1988	1990	15/12	229	112	LT42291121988350XXX03
1988	1990	20/01	223	111	LT42231111988020XXX01
1988	1990	10/02	226	112	LT42261121988041XXX04
1989	1990	11/01	223	112	LT42231121989070XXX02
1989	1990	24/01	221	112	LT42211121989024XXX03
1989	1990	24/01	221	113	LT42211131989024XXX03
1989	1990	09/02	4	111	LT40041111989040XXX02
1989	1990	09/02	1	111	LT40011111989035XXX03
1989	1990	09/02	4	113	LT40041131989040XXX02
1989	1990	13/03	4	113	LT40041131989072XXX02
1989	1990	12/12	219	112	LT42191121989346XXX04
1989	1990	21/12	1	111	LT40011121989355XXX02
1989	1990	21/12	1	112	LT40011111989355XXX02
1989	1990	21/12	1	113	LT40011131989355XXX01
1989	1990	24/12	223	112	LT42231121989358XXX02
1989	1990	26/12	4	111	LT40041121989360XXX02
1989	1990	26/12	4	112	LT40041111989360XXX02
1990	-	09/01	6	113	LT40061131990009XXX03
1990	-	24/01	232	112	LT42321121990024XXX04
1990	-	24/01	232	113	LT42321131990024XXX01
1991	1990	20/02	232	111	LT52321111991051XXX03
1991	1990	20/02	232	112	LT52321121991051XXX03
1991	1990	20/02	232	113	LT52321131991051XXX02
1999	2000	12/12	231	113	LE72311131999346AGS00
1999	2000	14/12	229	112	LE72291121999348AGS00
2000	-	01/01	227	112	LE72271122000001EDC00
2000	-	02/01	220	112	LE72201122001002EDC00
2000	-	03/01	229	111	LE72291112000063AGS00
2000	-	03/01	229	112	LE72291122000063AGS00
2000	-	07/01	4	111	LE70041112000007EDC00
2000	-	07/01	4	112	LE70041122000007EDC00
2000	-	07/01	4	113	LE70041132000007EDC00

Table S1. Landsat data used in the present study.

Year of Acquisition	*Circa Year*	*Day/Month (dd/mm)*	*Satellite Path #*	*Satellite Row #*	*Landsat ID #*
2000	-	09/01	2	111	LE70021112000009EDC00
2000	-	09/01	2	112	LE70021122000009EDC00
2000	-	11/01	233	111	LE72331112000011AGS01
2000	-	11/01	233	112	LE72331122000011AGS01
2000	-	12/01	224	111	LE72241112000012AGS00
2000	-	12/01	224	112	LE72241122000012EDC00
2000	-	16/01	220	111	LE72201112000016EDC00
2000	-	16/01	3	112	LE70031122000016AGS02
2000	-	20/01	232	113	LE72321132000020AGS00
2000	-	20/01	232	114	LE72321142000020EDC00
2000	-	21/01	6	111	LE70061112000021AGS00
2000	-	21/01	6	113	LE70061132000021AGS00
2000	-	24/01	228	111	LE72281112000024AGS00
2000	-	27/01	217	112	LE72171122000027EDC00
2000	-	28/01	217	112	LE72171122000059EDC00
2000	-	16/02	229	114	LE72291142000047EDC00
2000	-	17/02	3	113	LE70031132000048EDC00
2000	-	06/03	1	113	LE70011132000066EDC01
2000	-	06/03	1	114	LE70011142000066EDC00
2005	-	01/01	232	114	LE72321142005001EDC00
2005	-	02/01	223	112	LE72231122005002EDC00
2005	-	03/01	230	111	LE72301112005003EDC00
2005	-	03/01	230	112	LE72301122005003EDC00
2005	-	04/01	4	111	LE70041112005004ASN00
2005	-	04/01	4	112	LE70041122005004ASN00
2005	-	04/01	4	113	LE70041132005004ASN00
2005	-	05/01	228	111	LE72281112005005EDC00
2005	-	05/01	228	112	LE72281122005005EDC00
2005	-	06/01	2	111	LE70021112005006EDC00
2005	-	07/01	226	112	LE72261122005007EDC00
2005	-	08/01	233	111	LE72331112005008EDC00
2005	-	08/01	233	112	LE72331122005008EDC00
2005	-	08/01	217	112	LE72171122005008EDC00
2005	-	08/01	233	113	LE72331132005008EDC00
2005	-	08/01	233	114	LE72331142005008EDC00
2005	-	13/01	3	112	LE70031122005013EDC00
2005	-	13/01	3	113	LE70031132005013EDC00
2005	-	16/01	225	112	LE72251122005016EDC00
2005	-	21/01	228	111	LE72281112005021EDC00
2005	-	21/01	228	112	LE72281122005021EDC00
2005	-	22/01	2	112	LE70021122005022ASN00
2005	-	22/01	2	113	LE70021132005022ASN00
2005	-	22/01	219	112	LE72191122005022EDC01
2005	-	23/01	226	112	LE72261122005023EDC00
2005	-	24/01	233	111	LE72331112005024ASN00
2005	-	24/01	233	113	LE72331132005024ASN00

Table S1. Landsat data used in the present study. (Continued).

Year of Acquisition	*Circa Year*	*Day/Month (dd/mm)*	*Satellite Path #*	*Satellite Row #*	*Landsat ID #*
2005	-	24/01	233	114	LE72331142005024ASN00
2005	-	02/02	232	114	LE72321132005033EDC00
2005	-	03/02	232	114	LE72321142005033EDC00
2005	-	07/02	2	113	LE70021132005038EDC00
2005	-	07/02	2	114	LE70021142005038EDC00
2005	-	16/02	1	113	LE70011132005047EDC00
2005	-	18/02	232	113	LE72321132005049EDC00
2005	-	19/02	6	113	LE70061132005050ASN00
2010	-	01/01	230	111	LE72301112010001EDC00
2010	-	01/01	230	112	LE72301122010001EDC00
2010	-	02/01	4	111/4	LE70041112010002EDC00
2010	-	02/01	4	112/5	LE70041122010002EDC00
2010	-	02/01	4	113	LE70041132010002EDC00
2010	-	04/01	2	113	LE70021132010004ASN00
2010	-	09/01	222	111	LE72221112010009EDC00
2010	-	09/01	222	112	LE72221122010009EDC00
2010	-	10/01	229	112	LE72291122010010EDC00
2010	-	11/01	3	111	LE70031112010011EDC00
2010	-	15/01	232	111	LE72321112010015EDC00
2010	-	15/01	232	113	LE72321132010015EDC00
2010	-	15/01	232	114	LE72321142010015EDC00
2010	-	16/01	223	111	LE72231112010016EDC00
2010	-	16/01	223	112	LE72231122010016EDC00
2010	-	17/01	230	111	LE72301112010017EDC00
2010	-	17/01	230	112	LE72301122010017EDC00
2010	-	17/01	230	114	LE72301142010017EDC00
2010	-	18/01	4	111	LE70041112010018ASN00
2010	-	18/01	4	112	LE70041122010018ASN00
2010	-	18/01	4	113	LE70041132010018ASN00
2010	-	18/01	221	112	LE72211122010018EDC00
2010	-	18/01	221	113	LE72211132010018EDC00
2010	-	27/01	3	111	LE70031112010027ASN00
2010	-	28/01	227	112	LE72271122010028EDC00
2010	-	29/01	1	111	LE70011112010029ASN00
2010	-	29/01	1	112	LE70011122010029ASN00
2010	-	31/01	232	111	LE72321112010031EDC00
2010	-	02/02	2	111	LE70021112010036EDC00
2015	-	05/01	232	111	LC82321112015005LGN00
2015	-	05/01	232	112	LC82321122015005LGN00
2015	-	06/01	6	112	LC80061122015006LGN00
2015	-	06/01	143	132	LC81431322015006LGN00
2015	-	06/01	159	131	LC81591312015006LGN00
2015	-	06/01	223	111	LC82231112015006LGN00
2015	-	06/01	223	112	LC82231122015006LGN00
2015	-	07/01	230	111	LC82301112015007LGN00
2015	-	07/01	230	112	LC82301122015007LGN00

Table S1. Landsat data used in the present study. (Continued).

Year of Acquisition	*Circa Year*	*Day/Month (dd/mm)*	*Satellite Path #*	*Satellite Row #*	*Landsat ID #*
2015	-	08/01	221	112	LC82211122015008LGN00
2015	-	10/01	139	132	LC81391322015010LGN00
2015	-	15/01	142	131	LC81421312015015LGN00
2015	-	15/01	158	131	LC81581312015015LGN00
2015	-	15/01	222	112	LC82221122015015LGN00
2015	-	16/01	229	111	LC82291112015016LGN00
2015	-	16/01	229	112	LC82291122015016LGN00
2015	-	06/02	232	112	LC82321122015037LGN00
2015	-	06/02	232	113	LC82321132015037LGN00
2015	-	24/02	230	111	LC82301112015055LGN00
2015	-	24/02	230	112	LC82301122015055LGN00
2015	-	04/03	005	110	LO80051102015063LGN00
2015	-	04/03	222	112	LO82221122015063LGN00
2015	-	04/03	222	113	LO82221132015063LGN00
2015	-	05/03	229	112	LC82291122015064LGN00
2015	-	06/03	003	110	LC80031102015065LGN00
2015	-	06/03	228	112	LC82281122015265LGN00
2015	-	08/03	001	112	LC80011122015067LGN00
2015	-	08/03	001	113	LC80011132015067LGN00
2015	-	08/03	226	112	LC82261122015267LGN00
2015	-	13/03	004	111	LC80041112015072LGN00
2015	-	17/03	233	111	LC82331112015076LGN00
2015	-	17/03	233	112	LC82331122015076LGN00
2015	-	18/03	007	111	LC80071112015077LGN00
2015	-	19/03	231	111	LC82311112015078LGN00
2015	-	19/03	231	112	LC82311122015078LGN00
2015	-	27/03	223	111	LC82231112015086LGN00
2015	-	27/03	223	112	LC82231122015086LGN00

Table S1. Landsat data used in the present study. (Continued).

Sensor	*Spatial Resolution*[1] *(m)*	*Acquisition Date*	*Orbital Track*	*Region*	*Scene Centre*	
					PSX (m) [2]	*PSY (m)* [2]
ERS-1	4, 20	19940202	006	Western Abbot IS	-1868443	-329106
ERS-1	4, 20	19940205	006	Western Abbot IS	-1868443	-329106
ERS-1	4, 20	19940223	006	Western Abbot IS	-1868443	-329106
ERS-1	4, 20	19940226	006	Western Abbot IS	-1868443	-329106
ERS-1	4, 20	19940310	006	Western Abbot IS	-1868443	-329106
ERS-1	4, 20	19940313	006	Western Abbot IS	-1868443	-329106
ERS-1	4, 20	19920123	010	Western Abbot IS	-1849129	-275660
ERS-1	4, 20	19920126	010	Western Abbot IS	-1849129	-275660
ERS-1	4, 20	19920129	010	Western Abbot IS	-1849129	-275660
ERS-1	4, 20	19920201	010	Western Abbot IS	-1849129	-275660
ERS-1	4, 20	19940217	010	Western Abbot IS	-1849129	-275660
ERS-1	4, 20	19940220	010	Western Abbot IS	-1849129	-275660
ERS-1	4, 20	19940223	010	Western Abbot IS	-1849129	-275660
ERS-1	4, 20	19940226	010	Western Abbot IS	-1849129	-275660
ERS-2	4, 20	20110404	010	S. Abbot IS & N. Cosgrove IS	-1811915	-299155
ERS-2	4, 20	20110407	010	S. Abbot IS & N. Cosgrove IS	-1811915	-299155
ERS-2	4, 20	20110419	010	S. Abbot IS & N. Cosgrove IS	-1811915	-299155
ERS-2	4, 20	20110422	010	S. Abbot IS & N. Cosgrove IS	-1811915	-299155
ERS-2	4, 20	20110513	010	S. Abbot IS & N. Cosgrove IS	-1811915	-299155
ERS-2	4, 20	20110516	010	S. Abbot IS & N. Cosgrove IS	-1811915	-299155
ERS-2	4, 20	20110525	010	S. Abbot IS & N. Cosgrove IS	-1811915	-299155
ERS-2	4, 20	20110528	010	S. Abbot IS & N. Cosgrove IS	-1811915	-299155
ERS-1	4, 20	19940125	020	Southern Venable IS	-1780006	60229
ERS-1	4, 20	19940128	020	Southern Venable IS	-1780006	60229

Table S3. ERS-1/2 Synthetic Aperture Radar imagery used to make double-differential interferograms.

Sensor	*Spatial Resolution*[1] *(m)*	*Acquisition Date*	*Orbital Track*	*Region*	*Scene Centre*	
					PSX (m)[2]	*PSY (m)*[2]
ERS-1	4, 20	19940131	020	Southern Venable IS	-1780006	60229
ERS-1	4, 20	19940203	020	Southern Venable IS	-1780006	60229
ERS-1	4, 20	19940224	020	Southern Venable IS	-1780006	60229
ERS-1	4, 20	19940227	020	Southern Venable IS	-1780006	60229
ERS-1	4, 20	19920202	024	Fletcher Pen & Venable IS	-1912629	32447
ERS-1	4, 20	19920309	024	Fletcher Pen & Venable IS	-1912629	32447
ERS-1	4, 20	19920312	024	Fletcher Pen & Venable IS	-1912629	32447
ERS-1	4, 20	19940122	024	Eastern Abbot IS	-1835569	-35351
ERS-1	4, 20	19940125	024	Eastern Abbot IS	-1835569	-35351
ERS-1	4, 20	19940128	024	Eastern Abbot IS	-1835569	-35351
ERS-1	4, 20	19940131	024	Eastern Abbot IS	-1835569	-35351
ERS-1	4, 20	19940203	024	Eastern Abbot IS	-1835569	-35351
ERS-1	4, 20	19940221	024	Eastern Abbot IS	-1835569	-35351
ERS-1	4, 20	19940224	024	Eastern Abbot IS	-1835569	-35351
ERS-1	4, 20	19940227	024	Eastern Abbot IS	-1835569	-35351
ERS-1	4, 20	19940123	034	Southern Stange Ice IS	-1709336	351984
ERS-1	4, 20	19940126	034	Southern Stange Ice IS	-1709336	351984
ERS-1	4, 20	19940129	034	Southern Stange Ice IS	-1709336	351984
ERS-1	4, 20	19940201	034	Southern Stange Ice IS	-1709336	351984
ERS-1	4, 20	19940204	034	Southern Stange Ice IS	-1709336	351984
ERS-1	4, 20	19960118	052	Western Eltanin Bay	-1767678	193326
ERS-2	4, 20	19960119	052	Western Eltanin Bay	-1767678	193326
ERS-1	4, 20	19960222	052	Western Eltanin Bay	-1767678	193326
ERS-2	4, 20	19960223	052	Western Eltanin Bay	-1767678	193326
ERS-1	4, 20	19960120	081	Eastern Abbot IS	-1829616	-46596

Table S3. ERS-1/2 Synthetic Aperture Radar imagery used to make double-differential interferograms. (Continued).

Sensor	*Spatial Resolution*[1] *(m)*	*Acquisition Date*	*Orbital Track*	*Region*	*Scene Centre*	
					PSX (m)[2]	*PSY (m)*[2]
ERS-2	4, 20	19960121	081	Eastern Abbot IS	-1829616	-46596
ERS-1	4, 20	19960224	081	Eastern Abbot IS	-1829616	-46596
ERS-2	4, 20	19960225	081	Eastern Abbot IS	-1829616	-46596
ERS-1	4, 20	19960128	195	Eastern Eltanin Bay	-1733373	278510
ERS-2	4, 20	19960129	195	Eastern Eltanin Bay	-1733373	278510
ERS-1	4, 20	19960303	195	Eastern Eltanin Bay	-1733373	278510
ERS-2	4, 20	19960304	195	Eastern Eltanin Bay	-1733373	278510
ERS-1	4, 20	19960207	335	Eastern Abbot IS	-1879355	-336337
ERS-2	4, 20	19960208	335	Eastern Abbot IS	-1879355	-336337
ERS-1	4, 20	19960313	335	Eastern Abbot IS	-1879355	-336337
ERS-2	4, 20	19960314	335	Eastern Abbot IS	-1879355	-336337
ERS-1	4, 20	19960209	367	Western Eltanin Bay	-1804279	163064
ERS-2	4, 20	19960210	367	Western Eltanin Bay	-1804279	163064
ERS-1	4, 20	19960315	367	Western Eltanin Bay	-1804279	163064
ERS-2	4, 20	19960316	367	Western Eltanin Bay	-1804279	163064
ERS-1	4, 20	19960212	410	Venable IS & Western Eltanin Bay	-1816784	122938
ERS-2	4, 20	19960213	410	Venable IS & Western Eltanin Bay	-1816784	122938
ERS-1	4, 20	19960318	410	Venable IS & Western Eltanin Bay	-1816784	122938
ERS-2	4, 20	19960319	410	Venable IS & Western Eltanin Bay	-1816784	122938
ERS-1	4, 20	19960215	449	Central Eltanin Bay	-1772514	199407
ERS-2	4, 20	19960216	449	Central Eltanin Bay	-1772514	199407
ERS-1	4, 20	19960321	449	Central Eltanin Bay	-1772514	199407
ERS-2	4, 20	19960322	449	Central Eltanin Bay	-1772514	199407

[1]Spatial Resolution refers to SAR azimuth and range resolution, respectively. [2]Coordinates are Polar Stereographic WGS84 (-71º standard parallel).

Table S3. ERS-1/2 Synthetic Aperture Radar imagery used to make double-differential interferograms. (Continued).